ACS OMEGA

http://pubs.acs.org/journal/acsodf

Article

Rhamnolipid Biosurfactants for Oil Recovery: Salt Effects on the Structural Properties Investigated by Mesoscale Simulations

I-Chin Chen and Ming-Tsung Lee*

Cite This: *ACS Omega* 2022, 7, 6223−6237

Read Online

ACCESS | Metrics & More | Article Recommendations

ABSTRACT: Rhamnolipids (RLs) are biosurfactants produced by *Pseudomonas*. The biodegradability and the variety of their functionality make them suitable for environmental remediation and oil recovery. We use dissipative particle dynamics simulations to investigate the aggregation behaviors of ionic RL congeners with nonane in various operating conditions. Under zero-salinity conditions, all RL congeners studied here form small ellipsoidal clusters with detectable free surfactants. When salt ions are present, the electrostatic repulsion between the ionized heads is overcome, resulting in the formation of larger aggregates of unique structures. RLs with C10-alkyl tails tend to form elongated wormlike micelles, while RLs with C16-alkyl tails tend to form clusters in spherical symmetry, including vesicles. Di-rhamnolipids (dRLs) require stronger solvation than monorhamnolipids (mRLs) to form clusters, and the resulting size of micelles is decreased. The morphology of the mixed dRL/mRL/oil systems is controlled based on the type of the congeners and the oil contents. In addition, the divalent calcium ions are found to be influential to the structure of the micelles through different mechanisms. For 5 wt % salinity, the ionic RLs can form oil-swollen micelles up to a 1:1 surfactant-to-oil ratio, suggesting that ionic RLs are superb to act as cleaning agents for petroleum hydrocarbons in the marine area. These key findings may guide the design for RL-based washing techniques in enhanced oil recovery.

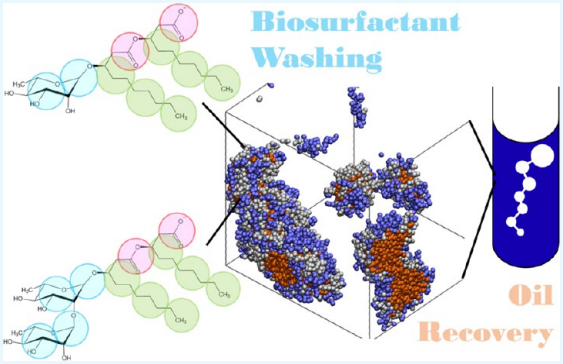

1. INTRODUCTION

Marine and soil pollution caused by petroleum hydrocarbons from the oil industry is a long-lasting issue to be resolved. The development of efficient and environmentally benign oil recovery technology is crucial to control and eliminate the waste oil in the ecosystem. Among the remediation treatments published by US EPA,[1] one of the most feasible ways to remove contaminations is surfactant washing, where the oil-containing reservoirs are flooded by surfactant solutions. The association of amphiphilic surfactants with hydrocarbons increases the corresponding solubility in water, thus making oil desorbed from the attached materials and removed from the contaminated sites.

For environmental sustainability, naturally derived biosurfactants are more desirable than synthetic ones because of their biodegradability and low toxicity.[2] Rhamnolipid (RL) is the most widely studied glycol-lipidic biosurfactant. A typical RL comprises one or two rhamnose heads, with one to three fatty acid chains being connected by ester bonds.[3,4] The fatty acid is composed of carboxyl acid and the alkyl chain with 8−16 carbon atoms. The variety of RL-producing microorganisms leads to diverse RL congeners whose molecular structures make them applicable to hydrocarbon and heavy metal remediation.[5−8]

The removal of hydrocarbons involves several mechanisms,[5,9,10] mobilization, which decreases the attachment between oil and its attached substances, solubilization, which increases the solubility of oil by accommodating it in the hydrophobic core of micelles, and emulsification, which packs oil into small droplets suspended in the water solution. In many studies, RL has shown its potential in these aspects compared to synthetic surfactants. Lai et al. found that RL out-perform Triton X-100 and Tween 80 in stimulating the mobilization of hydrocarbons from highly contaminated soil (9000 mg hydrocarbons/kg dry soil).[11] Ramirez et al. studied the performance of RL in recovering oil sludge compared with other commonly used surfactants such as Triton X-100 and X-114, Tween 80, and SDS. According to their study, RL has the oil recovery rate among the highest, which is around 40−70%. They have also found that the concentration of the surfactant used has a minimal effect on the oil recovery performance.[12] However, the application ratio of surfactant-to-oil (S/O) does have a great

Received: November 29, 2021
Accepted: January 28, 2022
Published: February 8, 2022

impact on the surfactant's performance in the presence of hydrocarbon as a cosolvent.

Although naturally produced RLs are usually in the form of mixtures of several congeners, specific congeners or tailored RLs can be synthesized currently.[13−15] The type of congeners also plays a role in hydrocarbon removal. Zhao et al. used three bacterial strains to produce RL solutions with various compositions of mono-RL (mRL) and di-RL (dRL). It is found that the emulsifying activity for crude oil is positively related to the portion of mRL, while the surface activity is positively related to the portion of dRL. Understanding the aggregation behaviors for each RL congener is therefore crucial to the future development of RL-based washing solutions.

Molecular modeling is a versatile way to gain a fundamental understanding of these mechanisms. The Schwartz group contributes several important MD investigations on nonionic[16] and ionic[17] forms of RL, including their applications in oil recovery.[18,19] There are also studies using atomistic[20] and coarse-grained simulations.[21] At the air−water interface, the conformation of the RL is found to be strongly dependent on the type of congeners.[20] The association between the polar carboxyl group and the rhamnose head leads to the closed conformation of the RL. This association is enhanced for ionic RL with the charged carboxyl group. However, both nonionic and ionic RLs prefer the open conformation for dRL congeners compared to mRL, possibly due to the steric hindrance caused by the extra sugar rings. If the lengths of the tails are different, asymmetric affinity to the water phase would be observed for the RL tails.[20] Moreover, the tails of dRL are elongated differently due to the second rhamnose head, in contrast to the tails of mRL.[19] All of these studies show that the structural characteristics, specifically the number of the head and the tail length, have subtle influences in controlling the conformation of the RL at the interface, which is related to their ability to alter the interfacial properties. In terms of interactions between the RL and oil molecules, Luft et al. studied the mixtures of Rha-C10-C10 and decane, and the RL can form stable oil-swollen micelles up to S/O of 2 based on their simulations and free energy calculations.[22]

Current simulation studies of RL focus on micellization in regular conditions with no salinity. However, in a current review, it is suggested that the efficiency of the RL in oil recovery depends on environmental factors.[23] The pH value, the ionic strength in the solution, and the concentration of RL in the liquid phase significantly affect the morphology of RL aggregates and consequentially impact the ability of RL aggregates in hydrocarbon removal. Because many oil reservoirs are immersed in the brine of different salinities, and the soil contains various kinds of heavy metals and charged complexes, it is essential to take a step toward the exploration of the aggregation behaviors of RL with hydrocarbons subjected to the influence of the ion valency and concentration. In such circumstances, the inclusion of the long-range electrostatic interactions makes it computationally expensive to perform systematic atomistic simulations. Since some of the unique micellar structures of RLs are difficult to achieve within the realistic simulation time scale using atomistic simulations,[16] it is more practical to employ a more efficient method of qualitative studying such as dissipative particle dynamics (DPD) simulation.

DPD has become a popular method in modeling amphiphilic self-assembly[24,25] following the theoretical development[26,27] and early simulations on surfactants.[28−32] Adjustments for interaction parameters and new parameterization schemes are constantly devised to improve the prediction for micellar and interfacial properties of common surfactants.[33−44] By smearing the point charge to a smooth distribution,[45,46] it is also possible to incorporate the calculation of electrostatic interactions using DPD to model the cationic and anionic surfactants correctly.[35,38,40] In the study of oil recovery using DPD, Bustamante-Rendón et al.[47] have investigated the decrease in the interfacial tension between water and oil with the addition of three different nonionic surfactants and the cationic DTAB. Simulations show that the ionic surfactant can reduce the surface tension better than the nonionic ones at a lower surfactant concentration. The phenomena are driven by the association of charged surfactant heads and the dissociated counter ions. Lee[21] investigated the morphologies of four common RL congeners and their aggregates with hydrocarbons. The morphologies of the aggregates vary from spherical, wormlike, to vesicular shapes depending on the chemical structure of congeners, the surfactant concentration, and the S/O ratio. All RL congeners are very efficient in associating with hydrocarbons, where the stable oil-swollen micelles are formed with nonane and pentadecane up to S/O equals 2. These observations are consistent with the atomistic simulations and the general reviews in the literature.

Overall speaking, the design of efficient RL-based washing fluid for oil recovery would require the aid of systematic studies from molecular perspectives. The RL-related research using molecular modeling is still in its infancy, and further investigation can be accelerated by reliable coarse-grained algorithms. Given our previously constructed force field for nonionic RL congeners,[21] this work explores the aggregation of hydrocarbons and four anionic RL congeners by the implementation of the smeared-charge method.[46] The details of the methodology, including the coarse-grained model, the force field, and the computational details, are shown in Section 2. Section 3 (Results and Discussion) is composed of several subsections: Section 3.1 reports the micellar properties of pure ionic RL solution. Section 3.2 reports the micellar properties of oil-swollen micelles containing nonane molecules at S/O equals 10. Four ionic RLs are studied in Sections 3.1 and 3.2 to compare the previous findings for their nonionic form.[21] Section 3.3 explores the oil-recovery performance of mixed mRL/dRL surfactant solutions. For each section, both normal conditions (only counter ions are added) and brine conditions (6 wt % salt are added) are studied to investigate the influences of ions in RL micellization. The chemical composition of brine is based on a recent study of oil recovery,[48] where the molar ratio of chloride ions (Cl^-), sodium (Na^+) ions, and divalent ions (Ca^{2+} and Mg^{2+}) are 53, 41, and 6%, respectively. Sections 3.4 and 3.5 report the effects of the oil content based on experimental observations.[12] Section 3.4 reports the micellar properties of oil-swollen micelles of Rha-C10-C10 and nonane at S/O ratios varying from 5 to 1. Section 3.5 reports the micellar properties of oil-swollen micelles of mixed Rha-C10-C10/dRha-C10-C10 and nonane at various S/O ratios. The influences of divalent ions on the micellization observed in many references (refs 48−51) are discussed in Section 3.6. All of the key findings are summarized in Section 4.

2. METHODOLOGY

2.1. Coarse-Grained Models and Force Field. Dissipative particle dynamics employed in this work is based on the development by Groot and Warren.[26] The theoretical background of the method and the force field can be found in refs 26, 27, 52−54. A simulation system is composed of highly populated coarse-grained (CG) beads, usually at the density of 3.[26,29] Each

https://doi.org/10.1021/acsomega.1c06741
ACS Omega 2022, 7, 6223−6237

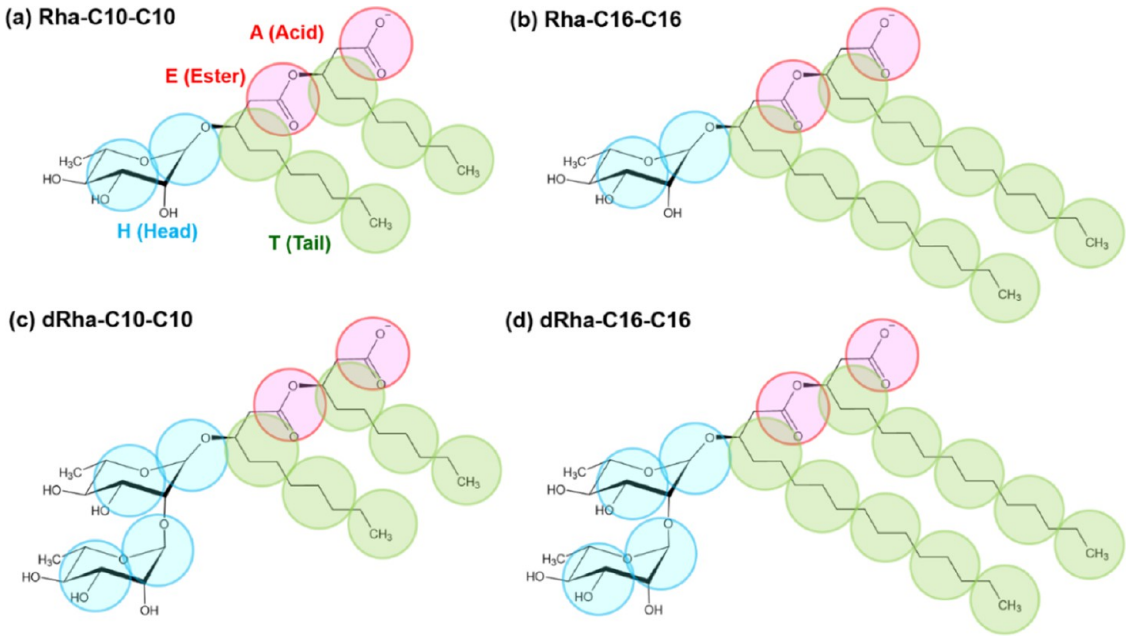

Figure 1. Chemical structures and the coarse-grained (CG) models for ionic RL congeners: (a) Rha-C10-C10, (b) Rha-C16-C16, (c) dRha-C10-C10, and (d) dRha-C16-C16. The CG bead types are introduced in Table 1.

bead represents several solvent molecules or a fragment of chain molecules. As illustrated in Figure 1, four RL congeners are modeled by bead-spring models, and the solvent or the solvated ions are also mapped to different beads based on Table 1.

Table 1. Mapping Between Atomistic and Coarse-Grained Beads

bead type	content	structure	charge	mass
	Surfactant			
T	alkyl tail	C_3H_8	0	1
HH dimer	rhamnose head	$C_6H_4O_4$	0	1
E	ester link	CH_3COO	0	1
A	carboxyl acid	CH_3COO^-	−1	1
	Solvent			
W	water	3 H_2O	0	1
I	hydrated sodium ion	Na^+·1.7 H_2O	1	1
J	hydrated chloride ion	Cl^-·H_2O	−1	1
K	hydrated calcium ion	Ca^{2+}·0.8 H_2O	2	1

The DPD beads interact via pairwise forces only within a short-ranged cutoff distance. The nonbonded forces and the bonded forces ($\mathbf{F}^B$) for a bead pair i and j are given in eq 1, where the nonbonded part includes the conservative forces ($\mathbf{F}^C$), the dissipative forces ($\mathbf{F}^D$), and the random forces ($\mathbf{F}^R$).

$$\mathbf{F}_{ij}(\mathbf{r}_{ij}) = \mathbf{F}_{ij}^B + \mathbf{F}_{ij}^C + \mathbf{F}_{ij}^D + \mathbf{F}_{ij}^R \quad (1)$$

The parameterization for dissipative forces and random forces follows the suggestions in the literature,[26] where the drag coefficient γ equals 4.5 (Table 2). Our current utilization focuses on the conservative forces and the bonded forces. For intramolecular interactions, the derivative of the standard harmonic potential in eq 2 is used for connecting the nearest bead neighbors (referred to as 1−2 bond) and the 2nd nearest bead neighbors (1−3 bond), which serves as the angle-term in common MD simulations. As given in eq 3, the conservative force is a soft repulsive one characterized by the repulsion

Table 2. Nonbonded and Runtime Parameters

a_{ij}	H	A/E	T	W/I/J/K
	Conservative Force			
H	25.00			
A/E	25.00	25.00		
T	55.09	39.45	25.00	
W/I/J/K	25.00	25.00	53.01	25.00
	Drag Force			
γ	4.50			
	Langevin Barostat			
P_0	23.70			
τ_P	0.50			
γ_P	10.00			
	SPME Electrostatic Interactions			
α	0.97			
k-vector	20	20	20	
β-spline	8			
Γ	13.87			
λ	0.25			

parameter a_{ij}, where r_{ij} is the center-to-center distance between bead i and j and r_c is the cutoff distance.

$$U_{ij}(r_{ij}) = \frac{K}{2}(r_{ij} - r_0)^2 \quad (2)$$

$$\mathbf{F}_{ij}^C = \begin{cases} a_{ij}\left(1 - \frac{r_{ij}}{r_c}\right)\frac{\mathbf{r_{ij}}}{r_{ij}}, & r_{ij} < r_c \\ 0, & r_{ij} \geq r_c \end{cases} \quad (3)$$

The repulsion parameters for the same bead type (i.e., $i = j$) determine the fluidic properties of the system,[26] and the repulsion parameters for different bead types drive the separation of the mesophase. As shown in Table 1, each bead type contains molecules of similar size and distinct functionality. The fatty acid in RL is modeled by a negatively charged acid

https://doi.org/10.1021/acsomega.1c06741
ACS Omega 2022, 7, 6223−6237

bead (type A) and the hydrophobic alkyl tail (type T), and each hydrophilic head is represented by a dimer (type H). An ester link (type E) is used to connect two fatty acid chains. Three water molecules are coarse-grained into a water bead (type W), and the ions of different valencies (type I for sodium ions, type J for chloride ions, and type K for calcium ions) are modeled in their hydrated forms to maintain the consistency of the bead volume. In our previous work for nonionic RL, a scale-bridging scheme is devised to parameterize the mismatch parameters in terms of activity coefficients of the bead components.[21] Following the literature approaches where the repulsion parameters scale with the solubility,[26,29] the repulsion parameters for mutually soluble pairs are set to be the same as the self-repulsion parameters. For insoluble bead pairs, the repulsion parameters are obtained by mapping the activity coefficient of the bead component to the calibration relations established by the particle insertion method,[55] where the activity coefficients are calculated by COSMOtherm[56,57] software and adjusted based on the solubility of water and alkane.[58] The repulsion parameters for this work are given in Table 2.

For charged bead pairs, we follow the approaches by Anderson et al.,[38] where the electrostatic interactions are calculated by the Slater-type charge smearing method[46] and the smooth particle mesh Ewald (SPME) algorithm.[59] To avoid the divergence of system energy while computing electrostatic potential with the soft-cored DPD forces (eq 3), the point charges located at the bead center are smeared by an exponential function.[46] Detailed formulas can be found in the Supporting Information of ref 38 and the user manual of DL_MESO software.[53,54] The parameters for long-range electrostatic interactions are given in Table 2, including the real-space convergence parameter α, the reciprocal space range k-vectors, and the maximum β-spline order. These parameters are chosen based on the examination in ref 38, where the relative errors in calculating electrostatic energies are below 1%. For short-range electrostatic interactions within the 3 r_c cutoff range,[45] the coupling constant Γ is decided based on the coarse-grained level as suggested in ref 45, and the smearing length λ equals 0.25 r_c based on our experiences in modeling proton exchange membranes.[60,61] More discussion about the choices of charge smoothing models and the parameterization on the screening properties can be found in ref 62, and the discussion about the Ewald parameters and the truncation errors should be referred to ref 63.

Bonded parameters are obtained based on the information collected from atomistic MD simulations. The hydrocarbon considered in this work is mainly nonane, which is modeled by three connected T beads. MD simulations of melted icosane at 1 atm and 473 K are first performed, and then the intramolecular distribution is obtained based on the coarse-grained mapping given in Table 1. DPD simulations of the homopolymer melt are carried out with adjustable bond parameters. The parameters that reproduce the molecular conformations as in the atomistic level using the coarse-grained model are given in Table 3. For surfactants, a similar approach is adapted to obtain the coefficients for 1−2 bonds and 1−3 bonds connecting different bead kinds. The reference MD simulation is performed on five dRha-C16-C16 molecules solvated in water, and the parameters that reproduce the conformations of RL are listed in Table 3 as well.

Computational details and the theoretical background for the above parameterizations can be found in our previous study.[21] The constructed force field has been validated by reproducing the self-assembled morphologies of a most common RL congener, Rha-C10-C10, obtained by MD simulations reported in the literature.[16] The formation of a spherical micelle, the transition of a spherical micelle to a wormlike micelle, and the vesicular formation have been captured by the DPD simulations. Based on this framework, we expand the parameter space to include charged particles for ionic RL and multivalent ions in the solutions.

Table 3. Bonded Parameters

bond type	r_0	K
Surfactant		
AT_{12}	0.444	450
ET_{12}	0.444	450
TT_{12}	0.521	800
TH_{12}	0.566	600
HH_{12}	0.651	300
$HH_{12'}$	0.389	2000
AT_{13}	1.080	30
ET_{13}	1.080	30
TT_{13}	1.412	40
AE_{13}	0.581	200
EH_{13}	0.691	120
HH_{13}	0.732	1600
Oil		
TT_{12}	0.500	360
TT_{13}	1.380	20

2.2. Computational Details. The simulations in this work are performed using version 2.7 revision 8 of the DL_MESO[53,54] DPD program. The cubic simulation box length equals 30 r_c., which corresponds to 19.4 nm based on the top-down mapping.[29] Simulations run 1.2 million steps at a 0.02 τ timestep, where the first 0.2 million steps are for equilibration. Five hundred configurations from the last 1 million steps are collected for further analysis. The constant-pressure−constant-temperature (NPT) ensemble uses a velocity Verlet integration thermostat and Langevin Barostat. The runtime parameters for the NPT ensemble, including the relaxation time and viscosity parameters, are given in Table 2, where the choices are based on the previous study.[21]

The characterization of the aggregation number is based on the code of Vishnyakov,[34] and the asphericity analysis is based on the homemade code.[33] The analysis for the distance distribution of tail configurations uses the RDF utility in MDynaMix[64] packages, version 5.2.8. The analysis for alkane molecular distributions is performed by the RDFMOL utility in the DL_MESO package, which calculates the radial distribution function of the centers of mass of the alkane molecules. Homemade programs for file handling and format conversion are used to convert VFT trajectories from DL_MESO[53] into XMOL trajectories for necessary analysis.

The asphericity[65] is used to quantify the geometry of the aggregates. Based on the coordinates of the beads belonging to an aggregate, the gyration tensor S_{ij} is first calculated using eq 4, where the superscript CM denotes the center of mass of the aggregate. The principal radii of gyration (R_1, R_2, and R_3) are obtained by solving S_{ij} for its eigenvalues. Finally, the radius of gyration R_g and the asphericity A are obtained using eqeqs 5 and eq 6. The value of A indicates the structure of the aggregate, where zero means a perfect sphere and unity means an infinitely long cylinder.

https://doi.org/10.1021/acsomega.1c06741
ACS Omega 2022, 7, 6223−6237

Table 4. Micellization of 6 wt % Surfactant in Water with 0 and 5 wt % Salinity

system composition[a]								
congener	N_{surf}	N_{oil}	N_W	N_{Na^+}	N_{Cl^-}	$N_{Ca_2^+}$	V [L]	C_{surf} [mM]
Rha-C10-C10	520	0	75 280	520	0	0	7.27×10^{-21}	118.7
Rha-C16-C16	390	0	75 150	390	0	0	7.27×10^{-21}	89.0
dRha-C10-C10	415	0	75 605	415	0	0	7.27×10^{-21}	94.8
dRha-C16-C16	325	0	75 475	325	0	0	7.28×10^{-21}	74.1
Rha-C10-C10	520	0	68 700	3180	3500	420	7.26×10^{-21}	118.9
Rha-C16-C16	390	0	68 570	3050	3500	420	7.26×10^{-21}	89.2
dRha-C10-C10	410	0	69 090	3070	3500	420	7.26×10^{-21}	93.8
dRha-C16-C16	325	0	68 895	2985	3500	420	7.26×10^{-21}	74.3
simulation results[b]								
$\langle R_g \rangle$	S.D.	$\langle A \rangle$	S.D.	morphology			$\langle N_{ag} \rangle$	CMC [mM]
5.3	1.3	0.37	0.15	ellipsoidal and rod-like			19	0.20
5.5	1.5	0.32	0.17	ellipsoidal and rod-like			24	0.00
5.0	0.2	0.32	0.03	ellipsoidal			14	0.32
4.8	0.2	0.32	0.02	ellipsoidal			9	0.05
10.5	0.9	0.24	0.03	wormlike, interconnected			335	0.05
9.3	2.2	0.34	0.27	vesicular and ellipsoidal			158	0.00
7.5	0.4	0.41	0.05	wormlike and ellipsoidal			56	0.16
6.7	0.2	0.37	0.05	ellipsoidal and rod-like			40	0.00

[a] N_{surf} is the number of the surfactant molecule, N_{oil} is the number of the oil molecule, N_W is the number of the water bead W, abd N_{Na^+}, N_{Cl^-}, and $N_{Ca_2^+}$ are the numbers of the ion beads. V is the average box size in the physical unit, which is used to calculate the concentration of surfactant C_{surf}. [b] $\langle R_g \rangle$ and S.D. are the average value and the standard deviation of the radius of gyration, respectively, $\langle A \rangle$ is the mean value of the asphericity, $\langle N_{ag} \rangle$ is the mean value of the aggregation number, and CMC is the critical micelle concentration. Tables 5−8 follow the same notation given here.

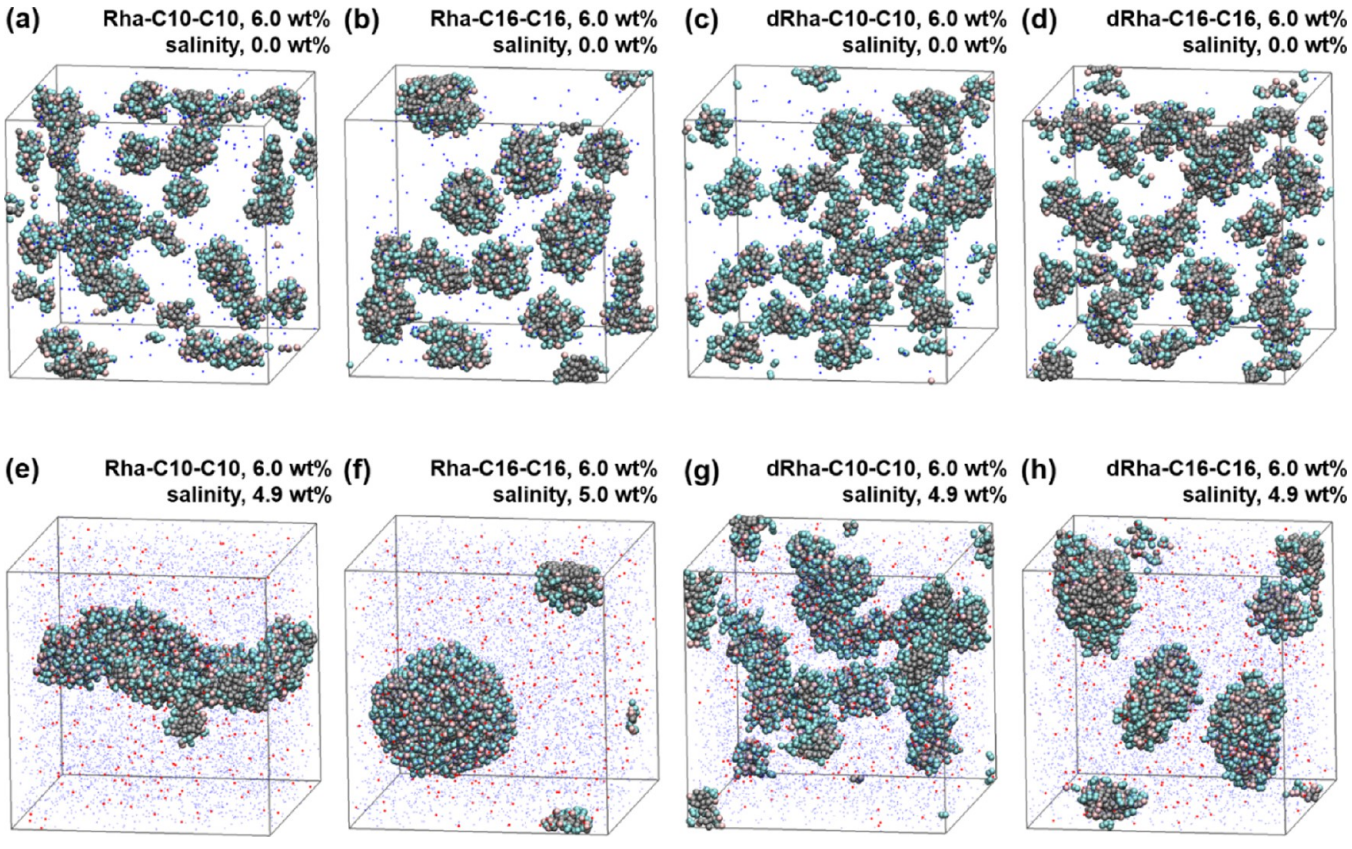

Figure 2. Micelles of 4 rhamnolipid congeners at 0 wt % (a−d) and at 5 wt % (e−h) salinity. The surfactant tails are in gray, head and ester link in cyan, and charged carboxyl groups in pink. Monovalent ions are represented by blue dots, and the divalent calcium ions are represented by red dots. Water is not shown for clarity.

https://doi.org/10.1021/acsomega.1c06741
ACS Omega 2022, 7, 6223−6237

Table 5. Oil-Swollen Micellization of 6 wt % Surfactant and 0.6 wt % Oil in Water with 0 and 5 wt % Salinity

system composition								
congener	N_{surf}	N_{oil}	N_W	N_{Na^+}	N_{Cl^-}	$N_{Ca_2^+}$	V [L]	C_{surf} [mM]
Rha-C10-C10	520	200	74 680	520	0	0	7.27×10^{-21}	118.8
Rha-C16-C16	390	200	74 550	390	0	0	7.27×10^{-21}	89.0
dRha-C10-C10	415	200	75 005	415	0	0	7.27×10^{-21}	94.8
dRha-C16-C16	325	200	74 875	325	0	0	7.28×10^{-21}	74.1
Rha-C10-C10	520	200	68 100	3180	3500	420	7.26×10^{-21}	119.0
Rha-C16-C16	390	200	67 970	3050	3500	420	7.25×10^{-21}	89.3
dRha-C10-C10	410	200	68 490	3070	3500	420	7.25×10^{-21}	93.9
dRha-C16-C16	325	200	68 295	2985	3500	420	7.25×10^{-21}	74.4
simulation results								
$\langle R_g \rangle$	S.D.	$\langle A \rangle$	S.D.	morphology				
5.7	1.6	0.37	0.15	ellipsoidal and rod-like				
6.0	0.7	0.33	0.08	ellipsoidal				
5.4	0.3	0.33	0.03	ellipsoidal				
5.2	1.2	0.32	0.11	ellipsoidal				
13.7	0.1	0.18	0.01	wormlike, interconnected				
9.7	0.4	0.23	0.11	vesicular and ellipsoidal				
7.5	1.3	0.32	0.09	wormlike and ellipsoidal				
7.0	0.1	0.33	0.11	ellipsoidal and rod-like				

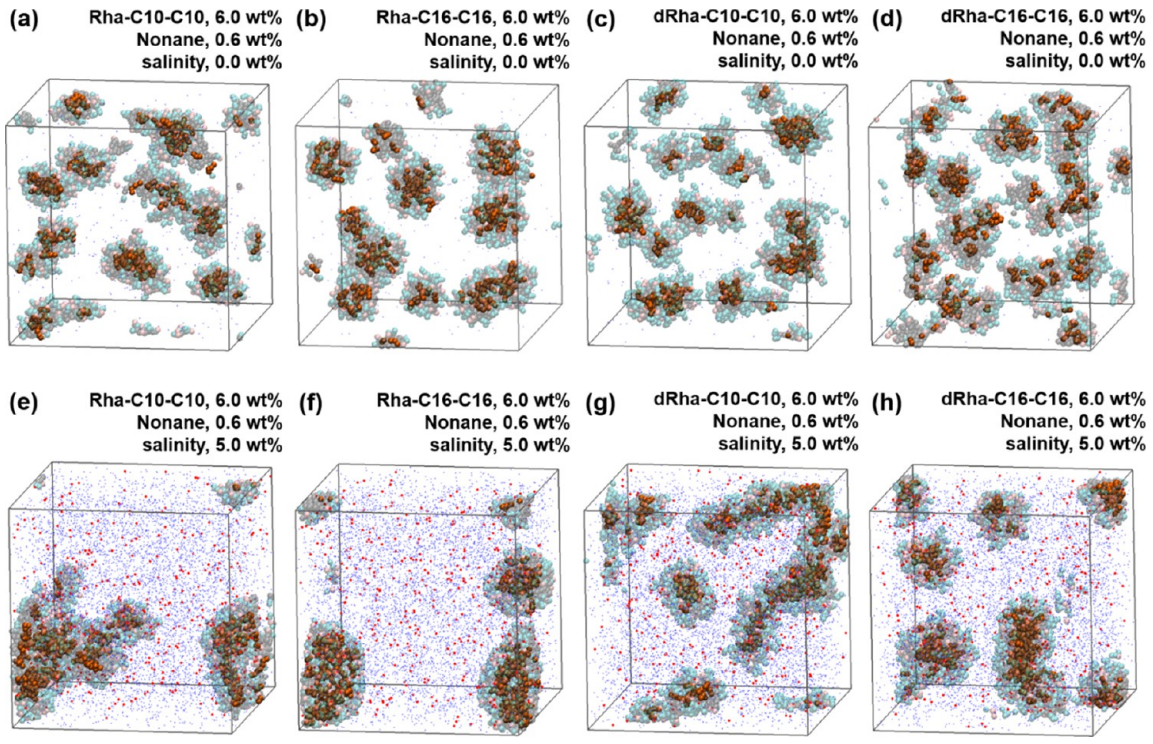

Figure 3. Oil-swollen micelles of 4 rhamnolipid congeners with nonane at 0 wt % (a–d) and at 5 wt % (e–h) salinity. The presentations of surfactants and salt ions are the same as in Figure 2, but the surfactants are drawn in a transparent style. Orange beads are nonane molecules.

$$S_{ij} = \frac{1}{N}\sum_{l=1}^{N}(S_{il} - S_i^{CM})(S_{jl} - S_j^{CM}) \quad (4)$$

$$R_g^2 = R_1^2 + R_2^2 + R_3^2 \quad (5)$$

$$A = \frac{1}{2R_g^4}[(R_1^2 - R_2^2) + (R_1^2 - R_3^2) + (R_3^2 - R_2^2)] \quad (6)$$

3. RESULTS AND DISCUSSION

3.1. Micellization of RL Congeners in Water and Brine.

The solutions which contain pure ionic RL with sodium counter ions are simulated to understand the RL self-assembly in terms of different congeners. For brine systems, monovalent and divalent ions are added to explore the salt effects. The concentrations of the RL (6 wt %) and the salinity (5 wt %) are chosen according to a recent study using ionic surfactants for the enhanced oil recovery operation.[48] The system compositions are given in Table 4. In the absence of added salts, the

https://doi.org/10.1021/acsomega.1c06741
ACS Omega 2022, 7, 6223−6237

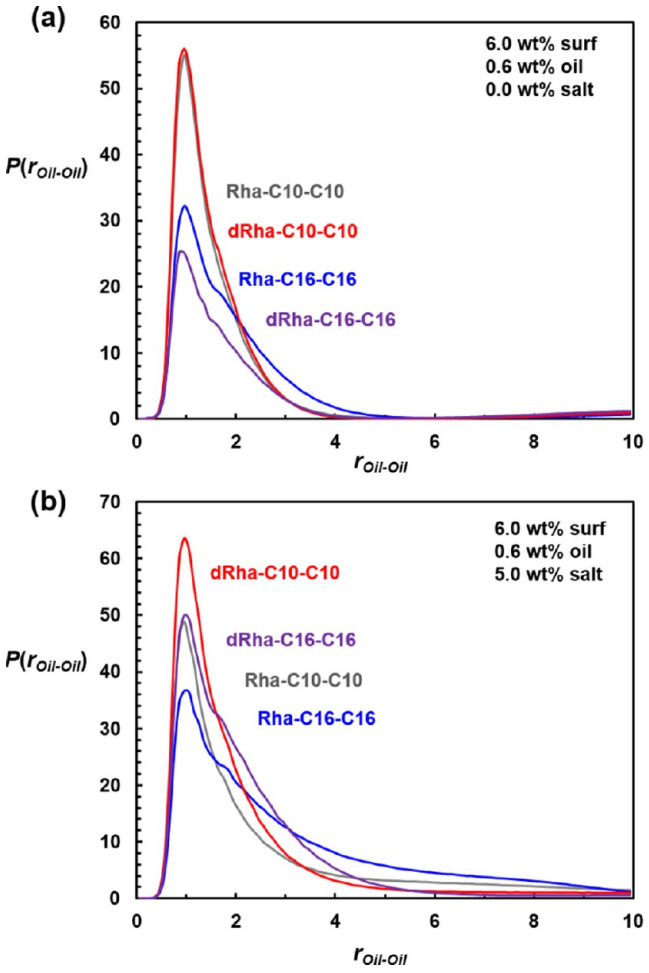

Figure 4. Radial distribution function of oil molecules (center of mass) in the oil-swollen micelle (S/O ratio equals 10) at (a) 0 wt % and (b) 5 wt % salinity. Color of the lines: Rha-C10-C10 in gray, Rha-C16-C16 in blue, dRha-C10-C10 in red, and dRha-C16-C16 in purple.

morphologies of aggregates formed by four RL congeners are very similar, as shown in Figure 2a–d. The bilipidic structure makes RL capable of forming premicelles with more than 10 molecules.[21] For the ionic Rha-C10-C10, most aggregates are small ellipsoids with rhamnose heads and charged acid beads being solvated by the surrounding water. The bicellar or rod-like-shaped aggregates of a larger size are also observed. Table 4 reports the corresponding average aggregation number N_{ag} equal to 19 and asphericity A around 0.37. The significant standard deviations of the radius of gyration R_g and A indicate the formation of bicelles. When the tail length is increased, Rha-C16-C16 forms a fewer number of micelles per simulation box (14 on average compared to 23 for Rha-C10-C10) with a larger size. The aggregates are still ellipsoidal and rod-like, but the shape is more spherical with a lower asphericity in Table 4. For dRha-C10-C10, the excess head beads require more solvation, and no bicelle is observed throughout the simulation. The associated standard deviations of R_g and A are diminished, as reported in Table 4. This head-group effect remains for dRha-C16-C16, but the longer tails provide a stronger hydrophobicity, resulting in the formation of smaller aggregates with a lower aggregation number. The effects of tail length and the head groups can also be rationalized by classical theory, such as the packing parameter.[66,67] For a surfactant in the aggregate, the packing parameter equals $v_0/a_e l_0$, where v_0 is the tail volume, a_e is its equilibrium area at the aggregate interface, and l_0 is the tail length. For both C10-RL and C16-RL, the strong hydrophobic interactions between the alkyl tails make them closely packed to each other. While packing the same number of surfactants in the aggregates, the growth of v_0 per surfactant molecules is smaller than that of l_0 for C16-RL compared to C10-RL. The lower packing parameter corresponds to the lower aggregation number and the spherical geometry for micelle, which is consistent with our observations. Overall speaking, the micellization of the ionic RL congeners in terms of their chemical structure is consistent with the previous investigation for their nonionic form.[21] Nevertheless, the aggregation numbers of ionic RL are much smaller than those of nonionic ones,[21] because of the barrier by the electrostatic repulsion between the charged head groups aligned at the aggregate interface.

For the brine systems, the presence of positively charged Na^+ and Ca^{2+} ions reduces the electrostatic repulsion between ionized head groups and hence allows the packing of more

Table 6. Oil-Swollen Micellization of Mixed 3 wt % Monorhamnolipid and 3 wt % Dirhmanolipid and 0.6 wt % Oil in Water with 0 and 5 wt % Salinity

system composition								
congener	N_{surf}	N_{oil}	N_W	N_{Na^+}	N_{Cl^-}	$N_{Ca_2^+}$	V [L]	C_{surf} [mM]
Rha-C10-C10	260	200	74 849	467	0	0	7.27×10^{-21}	59.4
dRha-C10-C10	207							47.3
Rha-C16-C16	195	200	74 721	357	0	0	7.28×10^{-21}	44.5
dRha-C16-C16	162							37.0
Rha-C10-C10	260	200	68 295	3125	3500	420	7.26×10^{-21}	59.5
dRha-C10-C10	205							46.9
Rha-C16-C16	195	200	68 141	3017	3500	420	7.25×10^{-21}	44.6
dRha-C16-C16	162							37.1

simulation results				
$\langle R_g \rangle$	S.D.	$\langle A \rangle$	S.D.	morphology
5.5	0.4	0.33	0.00	ellipsoidal
5.3	0.8	0.31	0.08	ellipsoidal
10.8	0.3	0.19	0.08	wormlike
8.3	3.8	0.31	0.26	vesicle and ellipsoidal

https://doi.org/10.1021/acsomega.1c06741
ACS Omega 2022, 7, 6223−6237

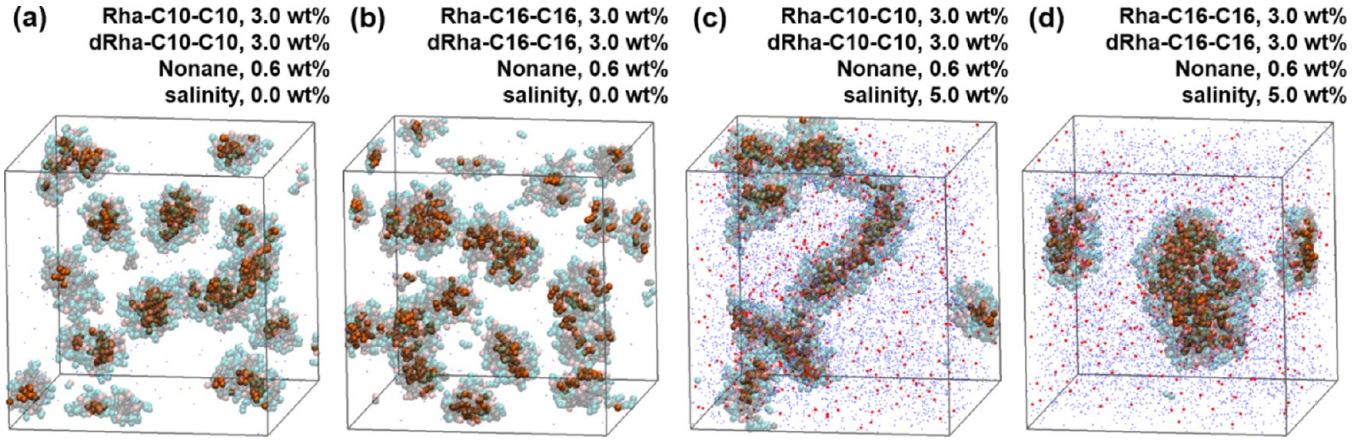

Figure 5. Oil-swollen micelles of mixed rhamnolipid congeners with nonane at 0 wt % (a, b) and 5 wt % (c, d) salinity. The presentations of surfactants and salt ions are the same as in Figure 2, but the surfactants are drawn in a transparent style. Orange beads are nonane molecules.

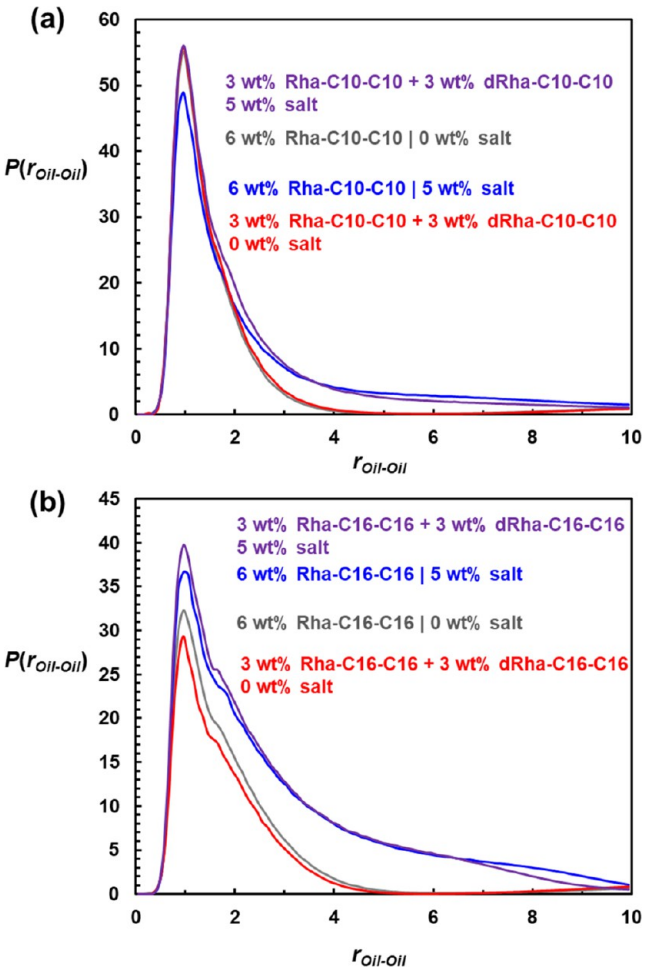

Figure 6. Radial distribution function of oil molecules (center of mass) in the oil-swollen micelle (S/O ratio of 10) at 0 wt % and 5 wt % salinity for (a) C10-RLs and (b) C16-RLs. Lines with different colors: gray, pure rhamnolipid solution at 0 wt % salinity; blue, pure RLs at 5 wt % salinity; red, mixed RL solution at 0 wt % salinity; and purple, mixed RL solution at 5 wt % salinity.

surfactant molecules in the aggregates. Compared to the water systems in Figure 2a−d, each RL congener form large aggregates of a unique morphology, as shown in Figure 2e−h. Rha-C10-C10 forms interconnected wormlike micelles in the brine system. Such morphology of elongated worm-like micelles which loop and network has also been observed for the nonionic dRha-C10-C10.[21] For Rha-C16-C16, a big unilamellar vesicle is formed along with a smaller spherical/ellipsoidal micelle. For dRha-C10-C10, while the wormlike micelles are still observed, the elongation of the micelles is limited. In contrast to Rha-C10-C10, mixed morphologies of small ellipsoidal, rod-like, and spiral-like aggregates are formed without observable loops or interconnected structures. For dRha-C16-C16, ellipsoidal aggregates are formed along with rod-like aggregates that are considerably shorter than the wormlike micelles of dRha-C10-C10.

In addition, we observe free surfactants in both water and brine systems. By calculating the average number of surfactants without interfering with any aggregates, the critical micelle concentrations (CMC) are reported in Table 4. For the zero-salinity case, CMC for Rha-C10-C10 is 0.2 mM, and the value increases to 0.32 mM for dRha-C10-C10. The substantial hydrophobicity of the long tail of Rha-C16-C16 and dRha-C16-C16 is more favorable to form micelles, and there are very few detectable free surfactants in the solution. The available experimental measurement on the CMC of the rhamnolipid is about 0.1−1 mM.[68,69] Although the experimentally produced rhamnolipids typically consist of several different rhamnolipid congeners, our predicted CMC is similar to the experimental CMC values of congeners. The amount of the free surfactants decreases when the salt concentration increases, which indicates that the alignment of charged head groups on the micelle−solution interface yields a lower energy for the surfactants.

3.2. Micellization of RL and Oil in Water and Brine.

Structural analysis of the oil-swollen micelle provides physical insights into the surfactant adsorption on the micro-oil drops in solutions. Similar to the conditions considered by Chen et al.,[48] about 0.6 wt % of modeled nonane is added to all of the systems discussed in Section 3.1, with the surfactant-to-oil ratio S/O being equal to 10. The system information and the simulation results are summarized in Table 5, and the corresponding visualizations are illustrated in Figure 3. In Figure 3a−d, the morphologies of the nonane-RL clusters at zero salinity are very similar to those in Figure 2a−d. The oil molecules are distributed in the hydrophobic subdomain of the micelle and packed with the surfactant tails. From the mean values and the standard deviations of the asphericity and radius of gyration reported in Table 5, the structures of oil-swollen micelles remain

https://doi.org/10.1021/acsomega.1c06741
ACS Omega 2022, 7, 6223−6237

Table 7. Oil-Swollen Micellization of 6 wt % Rha-C10-C10 with Oil at 1, 2, and 5 S/O Ratio and 0 and 5 wt % Salinity

system composition								
congener	N_{surf}	N_{oil}	N_W	N_{Na^+}	N_{Cl^-}	$N_{Ca_2^+}$	V [L]	C_{surf} [mM]
Rha-C10-C10	520	400	74 080	520	0	0	7.27×10^{-21}	118.8
Rha-C10-C10	520	1000	72 280	520	0	0	7.27×10^{-21}	118.8
Rha-C10-C10	520	2000	69 280	520	0	0	7.25×10^{-21}	119.0
Rha-C10-C10	520	400	67 500	3180	3500	420	7.25×10^{-21}	119.0
Rha-C10-C10	520	1000	65 700	3180	3500	420	7.24×10^{-21}	119.2
Rha-C10-C10	520	2000	62 700	3180	3500	420	7.22×10^{-21}	119.5
simulation results								
$\langle R_g \rangle$	S.D.	$\langle A \rangle$	S.D.	morphology				
5.8	0.6	0.33	0.04	ellipsoidal				
6.3	2.2	0.31	0.10	ellipsoidal				
7.2	0.9	0.33	0.14	ellipsoidal				
12.8	1.8	0.26	0.14	wormlike				
13.9	2.4	0.12	0.04	wormlike				
8.9	1.0	0.14	0.10	cylindrical				

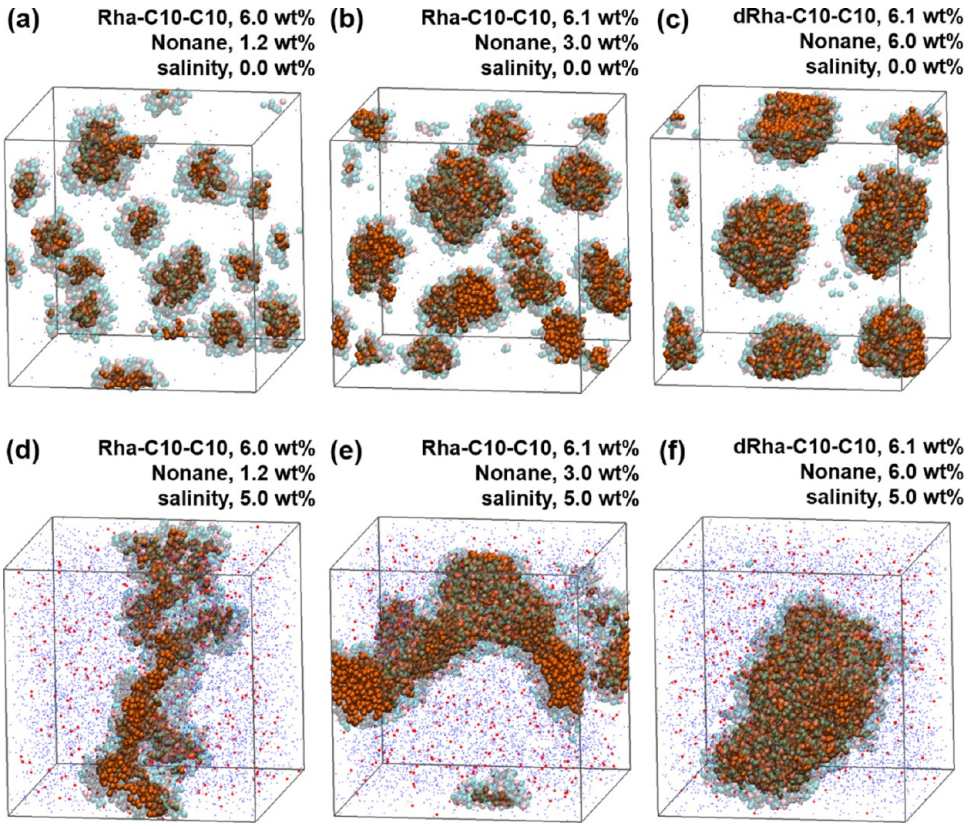

Figure 7. Oil-swollen micelles of Rha-C10-C10 with 1.2−6 wt % of nonane at 0 wt % (a−c) and at 5 wt % (d−f) salinity. The presentations of surfactants and salt ions are the same as in Figure 2, but the surfactants are drawn in a transparent style. Orange beads are nonane molecules.

similar to the pure RL systems, with only minor growth in the cluster size. In the brine conditions, the salt effect plays a similar role as in the pure RL cases. With the stabilization of the salt ions, the barrier at the micelle−solution interface caused by the electrostatic repulsion between charged head groups can be overcome, and the clusters grow in either length or size. The shape of the aggregates is still dominated by the tail length, where C16-RLs form spherical aggregates and C10-RL form elongated ones. It should be noted that the lower values of asphericity for Rha-C10-C10 in Tables 5 and 4 in the brine conditions have resulted from the secondary structure of the wormlike micelle, where the aggregates reside around the region confined by the simulation box and, therefore, decreases the asphericity.

By adding the nonane molecules, it is easier for RLs to form aggregates as the overall hydrophobicity of the system is increased. The resided oil molecules either aggregate as a hydrophobic core or pack with surfactants within the tail region based on the counter-balanced oil−oil and oil−surfactant interactions discussed in ref 70. For the zero-salinity cases, oil in the C10-RL micelles is visually closer to each other, especially in the spherical micelles. The distributions of the oil molecules are characterized by the RDFs for the center of the mass of the oil molecules. In Figure 4a, the C10-RLs have the higher peak for

https://doi.org/10.1021/acsomega.1c06741
ACS Omega 2022, 7, 6223−6237

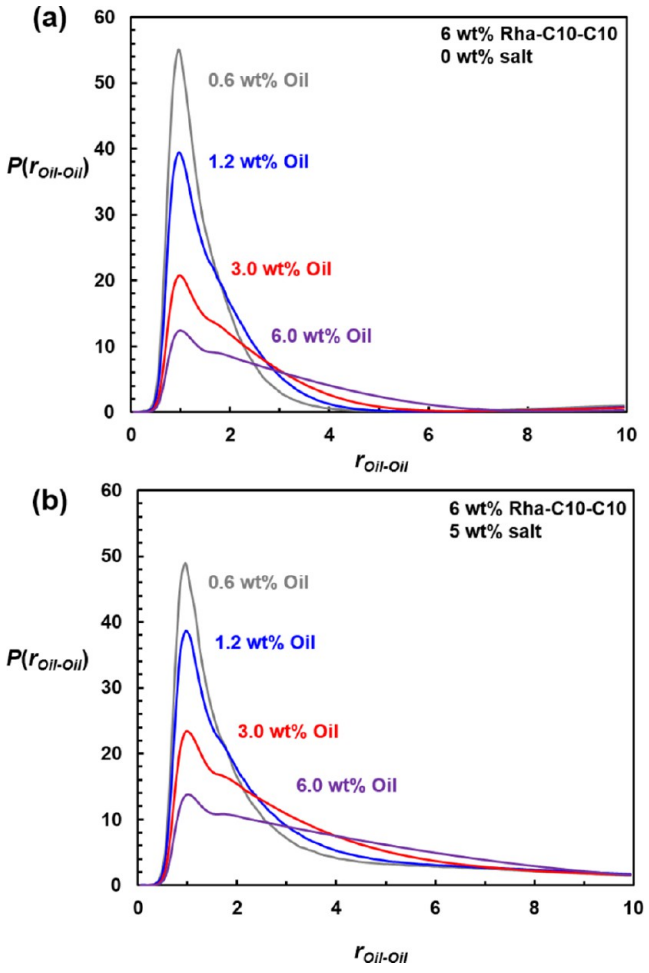

Figure 8. Radial distribution function of oil molecules (center of mass) in the oil-swollen micelle for 6 wt % of Rha-C10-C10 at salinity equal to (a) 0 wt % and (b) 5 wt %. Lines in different colors illustrate different oil contents: gray, 0.6 wt % nonane; blue, 1.2 wt % nonane; red, 3.0 wt % nonane; and purple, 6.0 wt % nonane.

the nearest oil pair, suggesting local aggregation of oil molecules. On the other hand, the oil−oil correlation length is generally longer in the micelles composed of C16-RLs. The peak for Rha-C16-C16 is slightly higher than dRha-C16-C16 because the RL aggregates are more isolated and well-dispersed such that oil molecules are more localized for Rha-C16-C16 (as shown in the S.D. of asphericity in Table 5). For the brine conditions, the oil distribution is affected by the distinct morphology of the micelles in Figure 3e−h. As shown in Figure 4b, the Rha-C16-C16 system shows the lowest peak for the oil−oil RDF due to the formation of the vesicle, where the oil molecules are distributed in the hydrophobic domain packed by the surfactant tails. The aggregation patterns for all of the other three congeners are similar, where small ellipsoidal aggregates agglomerate into wormlike shapes.

3.3. Micellization of Mixed RL and Oil in Water and Brine. To investigate the morphologies of aggregates formed by the mixed surfactants in the salt solution, we simulate the binary rhamnolipid congeners summarized in Table 6. 3 wt % of mRLs and 3 wt % of dRLs are mixed with 0.6 wt % oil, similar to the systems discussed in Table 5. Although the tail lengths of mRLs and dRLs are the same, the area of head groups in the mixed system is effectively increased compared to mRL−oil systems. As expected, the micellar structures of mRL/dRL/oil fall between the structure of mRL/oil and dRL/oil, as shown in Figure 5a−d. At zero salinity, most aggregates are small and ellipsoidal. The asphericity of the Rha-C10-C10/dRha-C10-C10/oil has the same value as dRha-C10-C10/oil, but the standard deviation is nearly zero, suggesting highly isolated clusters. The micelle structure of the Rha-C16-C16/dRha-C16-C16/oil is also similar to dRha-C16-C16/oil based on the radius of gyration and asphericity in Tables 5 and 6. For the brine conditions, Rha-C10-C10/dRha-C10-C10/oil forms wormlike micelles, as shown in Figure 5c, and the structural properties are dominated by the dRL. Nevertheless, in Figure 5d, the mixed C16-RL solution shows the morphology of a vesicle along with a spherical micelle, which is the same as Rha-C16-C16 in Figure 3f.

In Figure 6a,b, the effect of salt leads to long-range oil−oil correlations irrespective of surfactant compositions. The lower peak and longer range for the RDF of the Rha-C10-C10 system with 5 wt % salt in Figure 6a are consistent with the corresponding morphology in Figure 3e. Unlike the other RDFs in Figure 6a for systems forming micelles that are more isolated, the aggregate of Rha-C10-C10 with 5 wt % salt is larger in size, yielding more dispersed oil distribution in the aggregate. For the mixed C16-RLs, the oil distribution is largely dependent on the morphology of the micelle. The oil−oil correlation has the lowest peak when the aggregates are in the vesicular structure at 5 wt % salinity, and the peak is the highest for spherical micelles at 0 wt % salinity.

3.4. Micellization of RL and Excess Oil in Water and Brine. A recent study has shown that the surfactant-to-oil (S/O) ratio significantly influences the performance of oil recovery by surfactants, including RLs.[12] Here, we increase the amount of oil to 1.2, 3, and 6 wt %, which corresponds to S/O of 5, 2, and 1. The system information is summarized in Table 7, and the oil−surfactant assemblies are visualized in Figure 7, where we focus on Rha-C10-C10 surfactants for this part of the study. When there is no salt added, the oil molecules are packed into the hydrophobic core, which grows in size with the oil concentration, as shown in Figure 7a,b. The RL surfactants are adsorbed on the surface of the oil droplet, forming aggregates whose number decreases with an increase in the aggregate radius of gyration. When the salt is present, the ellipsoidal clusters agglomerate into wormlike micelles. The wormlike micelles are interconnected, as observed in the pure Rha-C10-C10 and Rha-C10-C10/oil systems. The cluster shape transforms gradually while retaining its wormlike structure with oil molecules being wrapped in the middle of the cluster. When the oil concentration increases to 3 wt %, the hydrophobic core of the wormlike micelle grows, as suggested by the oil−oil distribution function in Figure 8. As the oil content further increases to 6 wt %, the surfactant and oil first coagulate into 2−3 ellipsoidal micelles. These micelles later agglomerate into a bigger cluster with an irregular shape and finally form a cylindrical micelle. In general, the salt effects observed are consistent with the cases with lower S/O ratios. Four RL congeners considered are capable of wrapping nonane even at a S/O ratio as small as 1.

3.5. Micellization of Mixed RL and Excess Oil in Water and Brine. In this section, we explore the oil recovery performance of mixed surfactants with different S/O ratios. The visualization in Figure 9 shows that the mixed Rha-C10-C10/dRha-C10-C10/oil systems form similar structures as pure Rha-C10-C10/oil systems at zero salinity. The slightly lower S.D. and the higher radius of gyration of mixed surfactants in Table 8 indicate that the oil-swollen micelles are more uniform

https://doi.org/10.1021/acsomega.1c06741
ACS Omega 2022, 7, 6223−6237

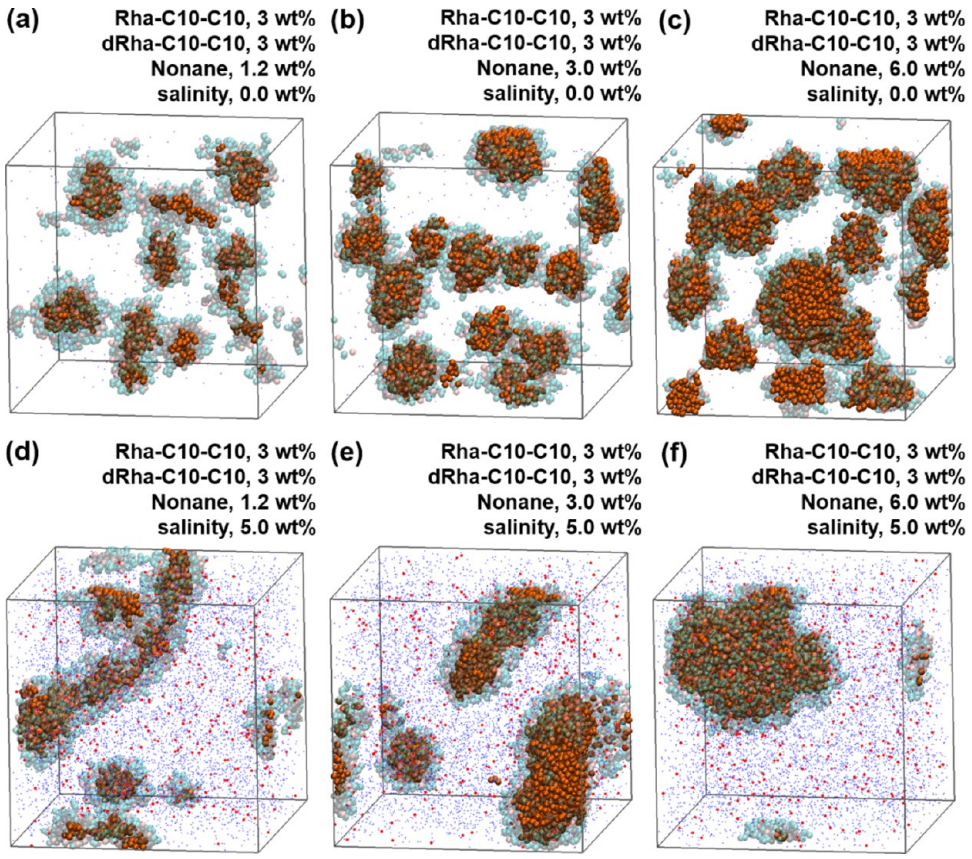

Figure 9. Oil-swollen micelles of Rha-C10-C10/dRha-C10-C10 mixtures with 1.2−6 wt % of nonane at 0 wt % (a−c) and at 5 wt % (d−f) salinity. The presentations of surfactants and salt ions are the same as in Figure 2, but the surfactants are drawn in a transparent style. The nonane molecules are shown in orange beads.

Table 8. Oil-Swollen Micellization of 6 wt % Rha-C10-C10/dRha-C10-C10 with Oil at 1, 2, and 5 S/O Ratios and 0 and 5 wt % Salinity

system composition								
congener	N_{surf}	N_{oil}	N_W	N_{Na^+}	N_{Cl^-}	$N_{Ca_2^+}$	V [L]	C_{surf} [mM]
Rha-C10-C10	260	400	74249	467	0	0	7.27×10^{-21}	59.4
dRha-C10-C10	207							47.3
Rha-C10-C10	260	1000	72449	467	0	0	7.26×10^{-21}	59.4
dRha-C10-C10	207							47.3
Rha-C10-C10	260	2000	69449	467	0	0	7.25×10^{-21}	59.5
dRha-C10-C10	207							47.4
Rha-C10-C10	260	400	67669	3127	3500	420	7.25×10^{-21}	59.5
dRha-C10-C10	207							47.4
Rha-C10-C10	260	1000	65869	3127	3500	420	7.24×10^{-21}	59.6
dRha-C10-C10	207							47.5
simulation results								
$\langle R_g \rangle$	S.D.		$\langle A \rangle$	S.D.		morphology		
5.7	0.6		0.34	0.06		ellipsoidal		
6.3	1.2		0.35	0.10		ellipsoidal		
8.3	0.7		0.40	0.07		ellipsoidal		
10.9	2.9		0.29	0.12		wormlike and ellipsoidal		
8.2	4.9		0.23	0.27		wormlike and ellipsoidal		
9.5	1.3		0.16	0.13		irregular		

in shape, which also suggests higher stability. In the presence of salt, the aggregates deviate from the wormlike shape in Rha-C10-C10/oil cases. At S/O of 5, wormlike micelles are formed along with some small ellipsoidal clusters. For S/O equal to 2, the clusters are rod-like or ellipsoidal. Nevertheless, the shape is less well-defined compared with Rha-C10-C10/oil systems. For S/O equal to 1, mRL/dRL molecules simply aggregate to form a big cluster. Similar to the observations in Section 3.3, the addition of the dRL increases the hydrophilicity of the systems, which drives

https://doi.org/10.1021/acsomega.1c06741
ACS Omega 2022, 7, 6223−6237

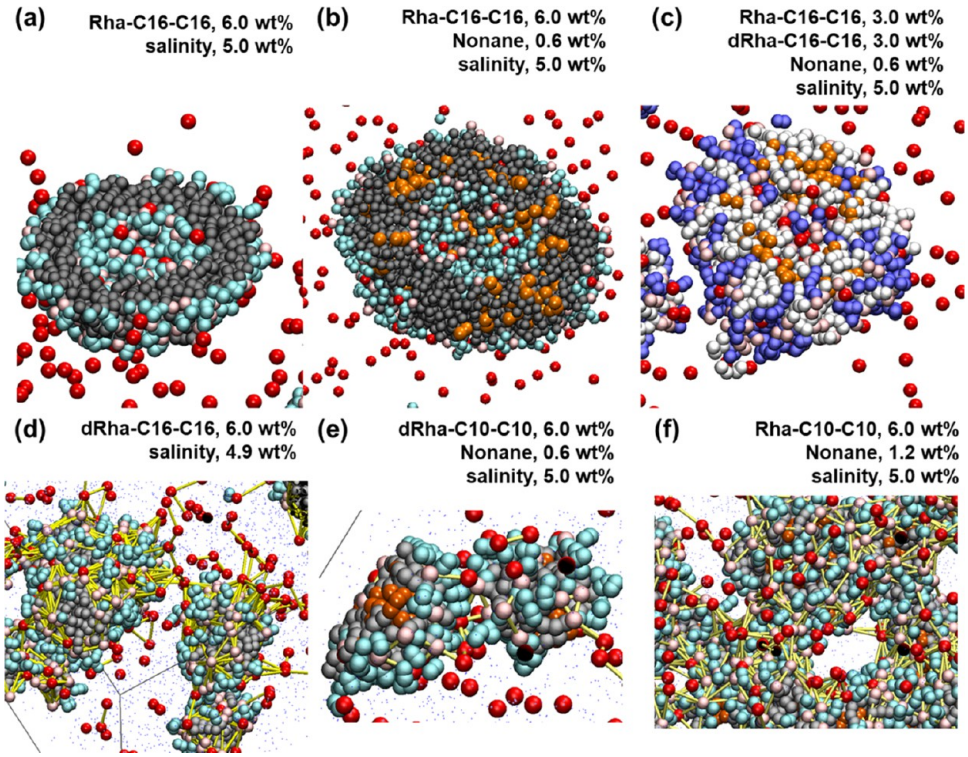

Figure 10. Association of calcium ions with the micelles. (a−c) Distribution of calcium ions (in red) in the vesicles. The presentation style for surfactants and oil is the same as in Figure 2, and oil is shown in orange. Panel (c) contains two types of surfactants, where mRL is shown in white and dRL is shown in purple. Dynamic bonds are drawn for calcium beads and acid beads. Panels (d)−(f) contain dynamic bonds in yellow bars, illustrating the association of nearby carboxyl acids and calcium ions within 3 r_c.

the formation of smaller aggregates as the extra head groups are better solvated.

3.6. Effects of Multivalent Ions. It is shown that multivalent ions have a dominant effect on the conformations of ionic surfactants, especially at the oil−water interface.[50] For all of the systems that mimic brine conditions in this study, the association between carboxyl acids and calcium ions is stronger than that between carboxyl acids and sodium ions. As illustrated in Figure 10a, most calcium ions (red beads) are distributed around the micelles, with some ions associated with the charged acid beads in the hydrophilic subdomain. Such characteristics are also found in the application of RL in contaminated soil washing, where the metal ions form complexes with RL.[23] Figure 10a−c illustrates the cross-sectional area of vesicles formed by pure and mixed RL with oil molecules. It is observed that the calcium ions are adsorbed in the hydrophilic subdomain both outside and inside of the hydrophobic subdomain of the vesicle. Therefore, calcium ions also contribute to the formation of micelles.

The distributed calcium ions between the two nearby aggregates also play a role in affecting the local structure and the formation of the equilibrium structure of micelles. As shown in Figure 10d−f, the yellow bars illustrate the association of nearby carboxyl acids and calcium ions within 3 r_c. The electrostatic attractions between the calcium ions and the carboxyl groups bridge the nearby aggregates, thus lowering the stability of the individual micelle, as shown in Figure 10d,e. Even for long, wormlike micelles presented in Figure 10f, the bridging effects of calcium ions and the hydrophilic domain of the micelles control the configuration in the aggregate. These interactions result in twisted wormlike micelles and the interconnective framework instead of elongated cylindrical micelles along one dimension. As also suggested by the structural analysis, the RL systems, especially with C10-tails, maintain a limited asphericity.

Figure 11a illustrates the distributions of calcium ions around the charged surfactant heads for pure RL solutions. The long tails of C16-RL drive the aggregation of spherical shape, which results in more populated negatively charged head groups at the micelle−solution interface. The alignment of the head groups leads to a higher local electronic density that attracts more calcium ions, as suggested by the higher peaks in Figure 11a. C10-RL systems tend to form wormlike aggregations, and the calcium ions are distributed between the nearby aggregates. As shown in Figure 11b, these behaviors are consistent with the systems at the S/O ratio of 10 for both pure RL and mixed RL solutions. To conclude, the calcium ions alter the local structure of the aggregates formed by different RL congeners, which may affect the surface-acting properties and mechanical properties.[71]

4. SUMMARY AND CONCLUSIONS

Dissipative particle dynamics simulations have been performed to predict the self-assembly of rhamnolipid surfactants and oil molecules in water and brine. Four RL congeners with different tail lengths and numbers of head groups are examined along with their mixtures. We explored the morphologies of oil-swollen micelles at different surfactant concentrations, surfactant-to-oil ratios, and salinities. The saline solution contains ions of multivalency to mimic the situation where oil recovery takes place in brine. Micellar properties are quantified based on the radius of gyration and the asphericity of the aggregates.

Simulation results show that all of the four congeners form small ellipsoidal aggregates in water with an aggregation number less than 25. The size of the aggregates grows with salinity as a

https://doi.org/10.1021/acsomega.1c06741
ACS Omega 2022, 7, 6223−6237

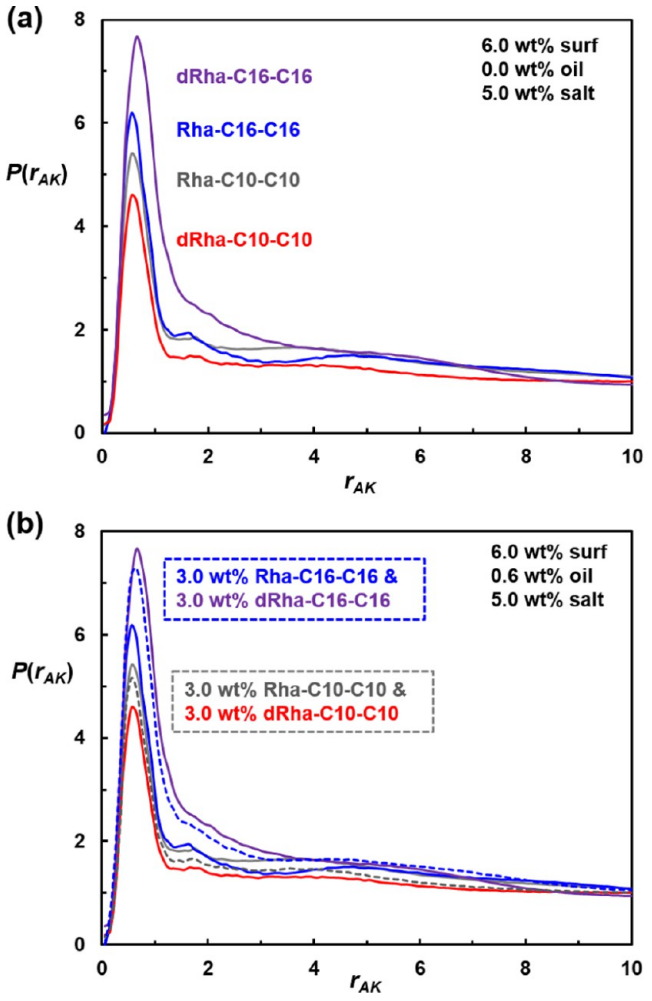

Figure 11. RDF of A bead (acid) and K bead (calcium) for (a) four different congeners in brine conditions (line colors are the same as those in Figure 4), and (b) oil-swollen micelle of pure and mixed RL solutions. Blue-dashed lines show the mixed C16-RL and C16-dRL, and the gray-dashed line shows the mixed C10-RL and C10-dRL.

result of the electrostatic interactions between the ionized heads. In the brine conditions, the micellar structure is dominated by the surfactant tail length, where the RLs with C10-tails tend to form elongated wormlike shapes, and RLs with C16-tails prefer the spherical clusters including vesicles. Regardless of the salinity, dRLs show much smaller aggregation numbers than RLs. The extra hydrophilic heads require more solvation, leading to a higher equilibrium area at the aggregate interface. Consequently, smaller clusters are formed, which agrees with the previous studies.[19,21,66]

In addition to the structure of the congeners, the divalent calcium ions are found to be influential to the morphologies of the aggregates. The bridging effects of the multivalent ions at the oil−surfactant−water interface[48−51] are observed. For small aggregates, the association between calcium ions and the charged surfactant heads decreases the stability of the individual micelle. However, it may lead to the formation of bicelles or wormlike micelles. The calcium ions around the elongated wormlike micelle also affect the growth of the micelle. For the vesicular clusters, calcium ions are adsorbed at both sides of the interface of the aggregates with the ionized heads. These phenomena are also found in the applications of RL for removing heavy metals in contaminated soil.

As oil is present in the system, RLs are able to form oil-swollen micelles. The nonane molecules are distributed in the hydrophobic subdomain and packed with the tails of the surfactant, while the micelles of each congener maintain their structure as in pure RL cases. All RL congeners have the ability to form oil-swollen aggregates for the S/O up to unity, and no dissociated oil molecules are observed in the solution. The aggregates of Rha-C10-C10 retain their ellipsoidal structure in the water systems and wormlike structures in the brine systems. When mixing mRL with dRL, the structures of the aggregates associated with oil fall between those of mRL/oil and dRL/oil, and the equilibrium morphologies are determined by the interplay of the congener structure and the composition of the RL mixtures. These observations may be helpful for designing future RL-based washing technology in the process of enhanced oil recovery.

AUTHOR INFORMATION

Corresponding Author

Ming-Tsung Lee − *Department of Chemical Engineering and Biotechnology, National Taipei University of Technology, Taipei 10608, Taiwan;* orcid.org/0000-0002-9326-8107; Email: mtlee@ntut.edu.tw

Author

I-Chin Chen − *Department of Chemical Engineering and Biotechnology, National Taipei University of Technology, Taipei 10608, Taiwan;* orcid.org/0000-0002-1504-6808

Complete contact information is available at: https://pubs.acs.org/10.1021/acsomega.1c06741

Notes

The authors declare no competing financial interest.

ACKNOWLEDGMENTS

This work was supported by the Ministry of Science and Technology (Taiwan) [Grant No. MOST 109-2221-E-027-058-MY3].

REFERENCES

(1) *Treatment Technologies for Site Cleanup: Annual Status Report*, Treatment Technologies for Site Cleanup: Annual Status Report (12th Edition).th ed.; U.S. Environmental Protection Agency (EPA), 2007.

(2) Patel, S.; Homaei, A.; Patil, S.; Daverey, A. Microbial biosurfactants for oil spill remediation: pitfalls and potentials. *Appl. Microbiol. Biotechnol.* **2019**, *103*, 27−37.

(3) Abdel-Mawgoud, A. M.; Lepine, F.; Deziel, E. Rhamnolipids: diversity of structures, microbial origins and roles. *Appl. Microbiol. Biotechnol.* **2010**, *86*, 1323−1336.

(4) Chen, J. W.; Wu, Q. H.; Hua, Y.; Chen, J.; Zhang, H. W.; Wang, H. Potential applications of biosurfactant rhamnolipids in agriculture and biomedicine. *Appl. Microbiol. Biotechnol.* **2017**, *101*, 8309−8319.

(5) Pacwa-Płociniczak, M.; Plaza, G. A.; Piotrowska-Seget, Z.; Cameotra, S. S. Environmental Applications of Biosurfactants: Recent Advances. *Int. J. Mol. Sci.* **2011**, *12*, 633−654.

(6) Chong, H. Q.; Li, Q. X. Microbial production of rhamnolipids: opportunities, challenges and strategies. *Microb. Cell Fact.* **2017**, *16*, No. 137.

(7) Fenibo, E. O.; Ijoma, G. N.; Selvarajan, R.; Chikere, C. B. Microbial Surfactants: The Next Generation Multifunctional Biomolecules for Applications in the Petroleum Industry and Its Associated Environmental Remediation. *Microorganisms* **2019**, *7*, No. 581.

(8) Mao, X. H.; Jiang, R.; Xiao, W.; Yu, J. G. Use of surfactants for the remediation of contaminated soils: A review. *J. Hazard. Mater.* **2015**, *285*, 419−435.

https://doi.org/10.1021/acsomega.1c06741
ACS Omega 2022, 7, 6223−6237

(9) Rosenberg, E.; Ron, E. Z. High- and low-molecular-mass microbial surfactants. *Appl. Microbiol. Biotechnol.* **1999**, *52*, 154−162.
(10) Urum, K.; Pekdemir, T. Evaluation of biosurfactants for crude oil contaminated soil washing. *Chemosphere* **2004**, *57*, 1139−1150.
(11) Lai, C. C.; Huang, Y. C.; Wei, Y. H.; Chang, J. S. Biosurfactant-enhanced removal of total petroleum hydrocarbons from contaminated soil. *J. Hazard. Mater.* **2009**, *167*, 609−614.
(12) Ramirez, D.; Shaw, L. J.; Collins, C. D. Oil sludge washing with surfactants and co-solvents: oil recovery from different types of oil sludges. *Environ. Sci. Pollut. Res.* **2021**, *28*, 5867−5879.
(13) Wittgens, A.; Rosenau, F. On the road towards tailor-made rhamnolipids: current state and perspectives. *Appl. Microbiol. Biotechnol.* **2018**, *102*, 8175−8185.
(14) Eslami, P.; Hajfarajollah, H.; Bazsefidpar, S. Recent advancements in the production of rhamnolipid biosurfactants by *Pseudomonas aeruginosa*. *RSC Adv.* **2020**, *10*, 34014−34032.
(15) Wittgens, A.; Rosenau, F.; et al. Heterologous Rhamnolipid Biosynthesis: Advantages, Challenges, and the Opportunity to Produce Tailor-Made Rhamnolipids. *Front. Bioeng. Biotechnol.* **2020**, *8*, No. 594010.
(16) Munusamy, E.; Luft, C. M.; Pemberton, J. E.; Schwartz, S. D. Structural Properties of Nonionic Monorhamnolipid Aggregates in Water Studied by Classical Molecular Dynamics Simulations. *J. Phys. Chem. B* **2017**, *121*, 5781−5793.
(17) Eismin, R. J.; Munusamy, E.; Kegel, L. L.; Hogan, D. E.; Maier, R. M.; Schwartz, S. D.; Pemberton, J. E. Evolution of Aggregate Structure in Solutions of Anionic Monorhamnolipids: Experimental and Computational Results. *Langmuir* **2017**, *33*, 7412−7424.
(18) Munusamy, E.; Luft, C. M.; Pemberton, J. E.; Schwartz, S. D. Unraveling the Differential Aggregation of Anionic and Nonionic Monorhamnolipids at Air-Water and Oil-Water Interfaces: A Classical Molecular Dynamics Simulation Study. *J. Phys. Chem. B* **2018**, *122*, 6403−6416.
(19) Luft, C. M.; Munusamy, E.; Pemberton, J. E.; Schwartz, S. D. A Classical Molecular Dynamics Simulation Study of Interfacial and Bulk Solution Aggregation Properties of Dirhamnolipids. *J. Phys. Chem. B* **2020**, *124*, 814−827.
(20) Euston, S. R.; Banat, I. M.; Salek, K. Congener-dependent conformations of isolated rhamnolipids at the vacuum-water interface: A molecular dynamics simulation. *J. Colloid Interface Sci.* **2021**, *585*, 148−157.
(21) Lee, M.-T. Micellization of Rhamnolipid Biosurfactants and Their Applications in Oil Recovery: Insights from Mesoscale Simulations. *J. Phys. Chem. B* **2021**, *125*, 9895−9909.
(22) Luft, C. M.; Munusamy, E.; Pemberton, J. E.; Schwartz, S. D. Molecular Dynamics Simulation of the Oil Sequestration Properties of a Nonionic Rhamnolipid. *J. Phys. Chem. B* **2018**, *122*, 3944−3952.
(23) Liu, G. S.; Zhong, H.; Yang, X.; Liu, Y.; Shao, B. B.; Liu, Z. F. Advances in applications of rhamnolipids biosurfactant in environmental remediation: A review. *Biotechnol. Bioeng.* **2018**, *115*, 796−814.
(24) Santo, K. P.; Neimark, A. V. Dissipative particle dynamics simulations in colloid and Interface science: a review. *Adv. Colloid Interface Sci.* **2021**, *298*, No. 102545.
(25) Español, P.; Warren, P. B. Perspective: Dissipative particle dynamics. *J. Chem. Phys.* **2017**, *146*, No. 150901.
(26) Groot, R. D.; Warren, P. B. Dissipative particle dynamics: Bridging the gap between atomistic and mesoscopic simulation. *J. Chem. Phys.* **1997**, *107*, 4423−4435.
(27) Español, P.; Warren, P. Statistical-mechanics Of Dissipative Particle Dynamics. *Europhys. Lett.* **1995**, *30*, 191−196.
(28) Shelley, J. C.; Shelley, M. Y. Computer simulation of surfactant solutions. *Curr. Opin. Colloid Interface Sci.* **2000**, *5*, 101−110.
(29) Groot, R. D.; Rabone, K. L. Mesoscopic simulation of cell membrane damage, morphology change and rupture by nonionic surfactants. *Biophys. J.* **2001**, *81*, 725−736.
(30) Prinsen, P.; Warren, P. B.; Michels, M. A. J. Mesoscale simulations of surfactant dissolution and mesophase formation. *Phys. Rev. Lett.* **2002**, *89*, No. 148302.
(31) Rekvig, L.; Kranenburg, M.; Vreede, J.; Hafskjold, B.; Smit, B. Investigation of surfactant efficiency using dissipative particle dynamics. *Langmuir* **2003**, *19*, 8195−8205.
(32) Yamamoto, S.; Hyodo, S. Mesoscopic simulation of the crossing dynamics at an entanglement point of surfactant threadlike micelles. *J. Chem. Phys.* **2005**, *122*, No. 204907.
(33) Lee, M. T.; Vishnyakov, A.; Neimark, A. V. Calculations of Critical Micelle Concentration by Dissipative Particle Dynamics Simulations: The Role of Chain Rigidity. *J. Phys. Chem. B* **2013**, *117*, 10304−10310.
(34) Vishnyakov, A.; Lee, M. T.; Neimark, A. V. Prediction of the Critical Micelle Concentration of Nonionic Surfactants by Dissipative Particle Dynamics Simulations. *J. Phys. Chem. Lett.* **2013**, *4*, 797−802.
(35) Mao, R. F.; Lee, M. T.; Vishnyakov, A.; Neimark, A. V. Modeling Aggregation of Ionic Surfactants Using a Smeared Charge Approximation in Dissipative Particle Dynamics Simulations. *J. Phys. Chem. B* **2015**, *119*, 11673−11683.
(36) Johnston, M. A.; Swope, W. C.; Jordan, K. E.; Warren, P. B.; Noro, M. G.; Bray, D. J.; Anderson, R. L. Toward a Standard Protocol for Micelle Simulation. *J. Phys. Chem. B* **2016**, *120*, 6337−6351.
(37) Lee, M. T.; Mao, R. F.; Vishnyakov, A.; Neimark, A. V. Parametrization of Chain Molecules in Dissipative Particle Dynamics. *J. Phys. Chem. B* **2016**, *120*, 4980−4991.
(38) Anderson, R. L.; Bray, D. J.; Del Regno, A.; Seaton, M. A.; Ferrante, A. S.; Warren, P. B. Micelle Formation in Alkyl Sulfate Surfactants Using Dissipative Particle Dynamics. *J. Chem. Theory Comput.* **2018**, *14*, 2633−2643.
(39) Danov, K. D.; Kralchevsky, P. A.; Stoyanov, S. D.; Cook, J. L.; Stott, I. P.; Pelan, E. G. Growth of wormlike micelles in nonionic surfactant solutions: Quantitative theory vs. experiment. *Adv. Colloid Interface Sci.* **2018**, *256*, 1−22.
(40) Panoukidou, M.; Wand, C. R.; Del Regno, A.; Anderson, R. L.; Carbone, P. Constructing the phase diagram of sodium laurylethoxysulfate using dissipative particle dynamics. *J. Colloid Interface Sci.* **2019**, *557*, 34−44.
(41) Johnston, M. A.; Duff, A. I.; Anderson, R. L.; Swope, W. C. Model for the Simulation of the CnEm Nonionic Surfactant Family Derived from Recent Experimental Results. *J. Phys. Chem. B* **2020**, *124*, 9701−9721.
(42) Lavagnini, E.; Cook, J. L.; Warren, P. B.; Williamson, M. J.; Hunter, C. A. A Surface Site Interaction Point Method for Dissipative Particle Dynamics Parametrization: Application to Alkyl Ethoxylate Surfactant Self-Assembly. *J. Phys. Chem. B* **2020**, *124*, 5047−5055.
(43) Del Regno, A.; Warren, P. B.; Bray, D. J.; Anderson, R. L. Critical Micelle Concentrations in Surfactant Mixtures and Blends by Simulation. *J. Phys. Chem. B* **2021**, *125*, 5983−5990.
(44) Šindelka, K.; Lisal, M. Interplay between surfactant self-assembly and adsorption at hydrophobic surfaces: insights from dissipative particle dynamics. *Mol. Phys.* **2021**, *119*, No. e1857863.
(45) Groot, R. D. Electrostatic interactions in dissipative particle dynamics-simulation of polyelectrolytes and anionic surfactants. *J. Chem. Phys.* **2003**, *118*, 11265−11277.
(46) González-Melchor, M.; Mayoral, E.; Velazquez, M. E.; Alejandre, J. Electrostatic interactions in dissipative particle dynamics using the Ewald sums. *J. Chem. Phys.* **2006**, *125*, No. 224107.
(47) Bustamante-Rendón, R. A.; Perez, E.; Goicochea, A. G. Comparing the efficiency of pure and mixed cationic and nonionic surfactants used in enhanced oil recovery by mesoscopic simulations. *Fuel* **2020**, *277*, No. 118287.
(48) Chen, H.; Gizzatov, A.; Abdel-Fattah, A. I. Molecular Assembly of Surfactant Mixtures in Oil-Swollen Micelles: Implications for High Salinity Colloidal Stability. *J. Phys. Chem. B* **2020**, *124*, 568−576.
(49) Underwood, T.; Erastova, V.; Cubillas, P.; Greenwell, H. C. Molecular Dynamic Simulations of Montmorillonite−Organic Interactions under Varying Salinity: An Insight into Enhanced Oil Recovery. *J. Phys. Chem. C* **2015**, *119*, 7282−7294.
(50) Riccardi, E.; Tichelkamp, T. Calcium ion effects on the water/oil interface in the presence of anionic surfactants. *Colloids Surf., A* **2019**, *573*, 246−254.

https://doi.org/10.1021/acsomega.1c06741
ACS Omega 2022, 7, 6223−6237

(51) Nan, Y.; Li, W.; Jin, Z. Ion Valency and Concentration Effect on the Structural and Thermodynamic Properties of Brine−Decane Interfaces with Anionic Surfactant (SDS). *J. Phys. Chem. B* **2021**, *125*, 9610−9620.
(52) Frenkel, D.; Smit, B. Dissipative Particle Dynamics. In. In *Understanding Molecular Simulation: From Algorithms to Applications*, 2nd ed.; Academic Press, 2002; pp; Chapter 17, pp 465−478.
(53) Seaton, M. A.; Anderson, R. L.; Metz, S.; Smith, W. DL_MESO: highly scalable mesoscale simulations. *Mol. Simul.* **2013**, *39*, 796−821.
(54) Seaton, M. A. DL_MESO_DPD: development and use of mesoscale modelling software. *Mol. Simul.* **2021**, *47*, 228−247.
(55) Widom, B. Some Topics in the Theory of Fluids. *J. Chem. Phys.* **1963**, *39*, 2808−2812.
(56) Klamt, A.; Eckert, F. COSMO-RS: a novel and efficient method for the a priori prediction of thermophysical data of liquids. *Fluid Phase Equilib.* **2000**, *172*, 43−72.
(57) Klamt, A.; Jonas, V.; Burger, T.; Lohrenz, J. C. W. Refinement and parametrization of COSMO-RS. *J. Phys. Chem. A* **1998**, *102*, 5074−5085.
(58) Shaw, D. G.; Maczynski, A.; Goral, M.; Wisniewska-Goclowska, B.; Skrzecz, A.; Owczarek, I.; Blazej, K.; Haulait-Pirson, M. C.; Hefter, G. T.; Kapuku, F.; et al. IUPAC-NIST solubility data series. 81. Hydrocarbons with water and seawater-revised and updated. Part 11. C-13-C-36 hydrocarbons with water. *J. Phys. Chem. Ref. Data* **2006**, *35*, 687−784.
(59) Essmann, U.; Perera, L.; Berkowitz, M. L.; Darden, T.; Lee, H.; Pedersen, L. G. A smooth particle mesh ewald method. *J. Chem. Phys.* **1995**, *103*, 8577−8593.
(60) Lee, M. T.; Vishnyakov, A.; Neimark, A. V. Coarse-grained model of water diffusion and proton conductivity in hydrated polyelectrolyte membrane. *J. Chem. Phys.* **2016**, *144*, No. 014902.
(61) Lee, M. T.; Vishnyakov, A.; Neimark, A. V. Modeling Proton Dissociation and Transfer Using Dissipative Particle Dynamics Simulation. *J. Chem. Theory Comput.* **2015**, *11*, 4395−4403.
(62) Warren, P. B.; Vlasov, A. Screening properties of four mesoscale smoothed charge models, with application to dissipative particle dynamics. *J. Chem. Phys.* **2014**, *140*, No. 084904.
(63) Vaiwala, R.; Jadhav, S.; Thaokar, R. Electrostatic interactions in dissipative particle dynamics-Ewald-like formalism, error analysis, and pressure computation. *J. Chem. Phys.* **2017**, *146*, No. 124904.
(64) Lyubartsev, A. P.; Laaksonen, A. M.DynaMix - a scalable portable parallel MD simulation package for arbitrary molecular mixtures. *Comput. Phys. Commun.* **2000**, *128*, 565−589.
(65) Rudnick, J.; Gaspari, G. The aspherity of random walks. *J. Phys. A* **1986**, *19*, No. L191.
(66) Israelachvili, J. N.; Mitchell, D. J.; Ninham, B. W. Theory of self-assembly of hydrocarbon amphiphiles into micelles and bilayers. *J. Chem. Soc., Faraday Trans. 2* **1976**, *72*, 1525−1568.
(67) Nagarajan, R. Molecular packing parameter and surfactant self-assembly: The neglected role of the surfactant tail. *Langmuir* **2002**, *18*, 31−38.
(68) Sánchez, M.; Aranda, F. J.; Espuny, M. J.; Marqués, A.; Teruel, J. A.; Manresa, A.; Ortiz, A. Aggregation behaviour of a dirhamnolipid biosurfactant secreted by *Pseudomonas aeruginosa*in aqueous media. *J. Colloid Interface Sci.* **2007**, *307*, 246−253.
(69) Chen, M.; Penfold, J.; Thomas, R.; Smyth, T.; Perfumo, A.; Marchant, R.; Banat, I.; Stevenson, P.; Parry, A.; Tucker, I. Mixing behavior of the biosurfactant, rhamnolipid, with a conventional anionic surfactant, sodium dodecyl benzene sulfonate. *Langmuir* **2010**, *26*, 17958−17968.
(70) Troncoso, A. B.; Acosta, E. Van der Waals free energy model for solubilization of oil in micelles. *Soft Matter* **2015**, *11*, 516−531.
(71) Riccardi, E.; Böhm, M. C.; Müller-Plathe, F. Molecular dynamics method to locally resolve Poisson's ratio: Mechanical description of the solid–soft-matter interphase. *Phys. Rev. E* **2012**, *86*, No. 036704.

https://doi.org/10.1021/acsomega.1c06741
ACS Omega 2022, 7, 6223−6237